JOURNAL OF SPACECRAFT AND ROCKETS
Vol. 60, No. 2, March–April 2023

Touchless Potential Sensing of Differentially Charged Spacecraft Using X-Rays

Julian Hammerl* and Andrea López†
University of Colorado Boulder, Boulder, Colorado 80303
Álvaro Romero-Calvo‡
Georgia Institute of Technology, Atlanta, Georgia 30332
and
Hanspeter Schaub§
University of Colorado Boulder, Boulder, Colorado 80303

https://doi.org/10.2514/1.A35492

A method has been proposed to estimate the electric potential of co-orbiting spacecraft remotely using x-rays that are excited by an electron beam. Prior work focused on the theoretical foundation and experimental validation of this approach using flat target plates. Although useful for concept validation, flat plates do not adequately represent the shape of spacecraft and the resulting complex particle dynamics. Additionally, all previous experiments employed fully conducting test objects, but it is not always possible to connect every spacecraft component to one common electric ground. This paper experimentally investigates the remote electrostatic potential estimation of objects with complex shapes and differentially charged components using x-rays. A particle tracing simulation framework is used to assist the interpretation of experimental results. The results show that the orientation of the target determines the areas irradiated by the electron beam and the detectability of different components. A new procedure is proposed to enable the simultaneous measurement of multiple potentials using a single x-ray spectrum, and dynamic experiments with a rotating target object are conducted to validate this method. The results of these dynamic experiments demonstrate that it is possible to estimate two potentials simultaneously with the support from theoretical x-ray models.

I. Introduction

SPACECRAFT charge in orbit due to various electric currents in the space environment. The incoming electromagnetic radiation from the sun induces the emission of photoelectrons from the surface of a satellite, which escape from the spacecraft if the craft is charged negatively, leading to a positive photoelectric current [1] (Chap. 7). The plasma environment in Earth orbit results in both positive and negative currents due to the ions and electrons that impact objects in space. In low Earth orbit (LEO), the plasma environment is cold (low particle energies, about 0.1 eV) and dense (densities of 10^5 cm^{-3} or higher) [1 (Chap. 1). Thus, spacecraft in LEO tend to charge to a maximum of a few volts positive in sunlight and a few volts negative in eclipse, but high electric potentials are possible when a charged beam is emitted from a spacecraft, when a spacecraft is at auroral latitudes during auroral activities, or during a few other distinct scenarios [1] (Chap. 1). In high Earth orbit, such as the Geostationary Earth Orbit (GEO) regime, however, the plasma is hot (energies in the keV level) and tenuous (densities less than 1 cm^{-3}), resulting in high spacecraft potentials that can reach tens of kilovolts [2]. These high electric potentials affect spaceflight in several different ways. One of these effects is arcing. It is recommended by spacecraft design guidelines to build fully conducting satellites in order to mitigate unfavorable charging effects [3] (Chap. 3). However, if the spacecraft is not fully conducting, some components charge to different potentials than others, referred to as differential charging. This can lead to arcing between components, e.g., between the solar panel and the spacecraft bus, and consequently reduces the lifetime of the solar panel and the spacecraft [4,5]. Electrostatic discharge can also occur during docking operations if the electric potential difference between the two objects is large. This is possible if one spacecraft eclipses the other while docking, blocking out the light from the sun that is responsible for the photoelectric current. For instance, the Lunar Gateway is expected to be oriented such that the Orion capsule's tail faces the sun during docking operations [6], which can lead to hazardous spacecraft charging events if the Orion capsule eclipses parts of the Lunar Gateway.

Another consequence from spacecraft charging is the electrostatic forces that result from electric potentials. Two charged objects in proximity are subject to electrostatic forces proportional to the charging levels of the two objects. While opposite signs of the charges result in attractive forces, equal signs cause repelling forces. Thus, even if both objects are charged to the same potential, they are subject to a repelling force. This also leads to electrostatic torques if the center of charge of each object does not correspond to its center of mass [7,8]. These electrostatic forces and torques can drastically influence the relative motion during rendezvous and proximity operations as well as docking [7]. By remotely estimating the electric potential of nearby spacecraft, one can feed-forward the expected electrostatic forces to reduce the control effort [9]. One can also take advantage of charged spacecraft and the resulting forces and torques. The Electrostatic Tractor concept utilizes the electrostatic force to touchlessly relocate retired satellites from GEO to a graveyard orbit [10]. The proposed relative motion control of the servicing satellite depends on the electric potential of the debris and consequently benefits from electric potential estimation [11]. While it would be possible to establish contact between the servicing satellite and the debris to measure the potential difference (the voltage) directly, this would conflict with the fundamentally contactless approach of the Electrostatic Tractor concept. Thus, remote electric potential

Presented as Paper 2022-2312 at the AIAA SciTech 2022 Forum and Exposition, San Diego, CA, January 3–7, 2022; received 17 June 2022; revision received 20 October 2022; accepted for publication 31 October 2022; published online 28 November 2022.

*Graduate Research Assistant, Ann and H. J. Smead Department of Aerospace Engineering Sciences; julian.hammerl@colorado.edu. Student Member AIAA.

†Graduate Research Assistant, Ann and H. J. Smead Department of Aerospace Engineering Sciences. Student Member AIAA.

‡Assistant Professor, Daniel Guggenheim School of Aerospace Engineering. Member AIAA.

§Professor and Glenn L. Murphy Chair of Engineering, Ann and H. J. Smead Department of Aerospace Engineering Sciences. Fellow AIAA.

sensing of nearby spacecraft has clear benefits for human and robotic spaceflight.

Several methods to remotely sense electric potentials have been proposed. While it is possible to use x-ray, optical, and radio emissions from GEO satellites to detect spacecraft charging and arcing events from LEO and even from Earth's surface [12], the proposed method only indicates that a spacecraft is charged, but not to what level. Bennett [13] proposes to estimate the electric potential of a nearby spacecraft from the relative motion evolution due to the perturbation by the electrostatic force between the two craft. However, the estimation accuracy of this method depends on the accuracy of the gravitational and relative motion models, only the potential of an effective sphere model is estimated, and it takes minutes to hours to update the charge estimate. Engwerda [14] proposes to estimate the electric potential and create a multisphere model (MSM, see Ref. [15]) by measuring the electric field around the spacecraft, but the study neglects the challenges of measuring an electric field in a tenuous plasma environment [16].

Two new methods to sense electric potentials of nearby spacecraft have been investigated in recent years: the electron method [17] and the x-ray method [18]. The electron method employs a servicing spacecraft equipped with an electron beam that is aimed at a nearby object of interest. When electrons impact on a surface, they excite secondary electrons that leave the surface with nearly zero kinetic energy and are accelerated if the object is charged negatively. The kinetic energy of the electrons when they arrive at a servicing spacecraft corresponds to the potential difference between the object and the servicer. Thus, by measuring the energy of the secondary electrons with a servicing satellite at a known potential, the electric potential of the object is inferred. The x-ray spectroscopy method utilizes an electron beam on a servicing spacecraft to excite x-rays on a nearby object, as illustrated in Fig. 1. Bremsstrahlung radiation is emitted from the object at a continuous spectrum of energies, and the maximum energy of the recorded spectrum corresponds to the landing energy of the impacting electrons. If the object is charged positively or negatively, the electrons are either accelerated or decelerated before they arrive at the object, which increases or decreases the maximum energy of the x-ray spectrum. Thus, measuring the potential of the servicing spacecraft using a langmuir probe [19] and knowing the initial energy of the electrons (the electron beam energy), the electric potential of the object is estimated. Both methods have been validated experimentally [20,21] for terrestrial conditions in the Electrostatic Charging Laboratory for Interactions between Plasma and Spacecraft (ECLIPS) research vacuum chamber [22]. This work focuses on the x-ray method.

Prior research developed the theoretical foundation for touchlessly determining electric potentials using x-ray spectroscopy [18]. The x-ray spectrum consists of characteristic radiation at discrete energies and continuous Bremsstrahlung radiation. Characteristic radiation is emitted at an energy that is distinct for each element, so the x-ray method can also be used for determining material composition [18]. The x-ray method is experimentally validated in Ref. [21], where it is shown that it is possible to estimate electric potentials of a flat plate with errors of less than 100 V for a wide range of potentials and for various angles between the x-ray detector and the electron beam. Wilson [23] investigates the angular dependence of the x-ray method by conducting experiments with a rotating target plate and also by changing the angle between the detector and the electron beam. The results suggest that there is no relationship between the accuracy of this method and the angle of the target plate or the x-ray detector, but the number of photons detected by the x-ray detector (the signal availability) is affected by the plate angle. Wilson [23] also shows that the accuracy of this method for the given x-ray detector decreases with increasing electron landing energy due to saturation of the detector, and suggests to control the electron beam energy as a function of the potential of the object (and of the servicing satellite, because the relative potential between the two objects determines the landing energy) to maintain a constant landing energy and enable better potential estimation. Wilson et al. [24] propose to use the x-rays that are generated by the ambient plasma environment to passively determine the potential of a nearby object without using an active electron beam. The proposed method was tested experimentally [24] in a vacuum chamber using a broad-spectrum electron gun [25] that emits electrons of multiple energies at the same time.

However, all experiments for the x-ray method were conducted with a single flat plate that is homogeneously charged to a single potential. Thus, the effects of complex-shaped objects and differentially charged components on the performance of the x-ray remote sensing method were not studied. This paper investigates the remote electric potential estimation of objects with complex shapes and differentially charged components by performing experiments in a vacuum chamber. The goal is to find the relationship between the target orientation and the observability of the potential of each component. An overview of the experimental setup and the particle tracing simulation framework used in this work is provided in Sec. II, as well as a fundamental review of the x-ray spectroscopic potential estimation method. The experimental results are shown in Sec. III. Two different approaches are discussed: the first approach aims at measuring the potential of each component of the target object individually, while the second strategy seeks to measure multiple potentials simultaneously. The observability of each component as a function of the target orientation is also discussed.

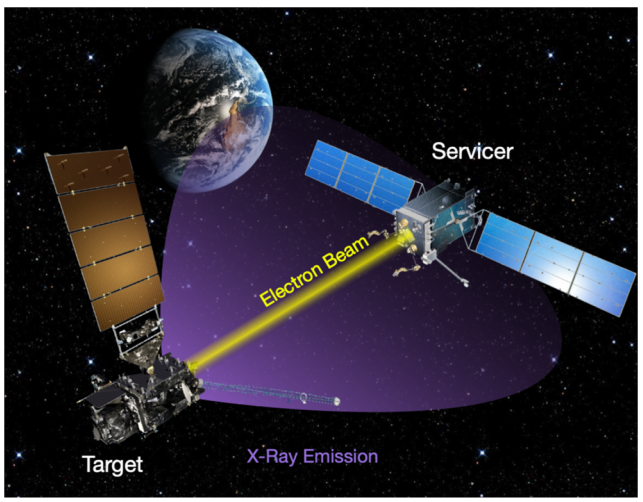

Fig. 1 Concept of touchlessly sensing the electric potential of a nearby object using the x-ray method.

II. Theory of Potential Estimation Using X-Rays and Experimental Setup

A. Theory of X-Ray Spectroscopic Potential Estimation

Energetic electrons can interact with atoms in various ways. When an inner-shell electron is removed by an incoming energetic electron, an outer-shell electron of the atom fills the vacant spot of the inner shell, and the difference in energy between the two shells is released as a characteristic x-ray photon [26] (Chap. 10). Because the energy difference between shells varies from element to element, the characteristic energy is specific to each element and allows for material identification. Another type of interaction occurs when an electron traverses closely to an atomic nucleus and is decelerated. Again, the loss in energy is emitted as an x-ray photon, called Bremsstrahlung (German for braking radiation) [26]. However, because the interaction with the nucleus can occur in many different paths, the energy of the emitted x-ray is not distinct as for characteristic x-rays, but continuous. The maximum Bremsstrahlung energy is given by the Duane–Hunt law and is equal to the energy of the incident electron before the interaction with the atom [27], referred to as the landing energy (or effective energy). Thus, x-ray spectra can be used to estimate the landing energy of the electron beam electrons. The electron beam interacts with the electric field created by charged objects, and the change in kinetic energy of the electron beam corresponds to the difference in electric potential between the serving satellite (the initial location of the electron beam electrons) and the target object (the final location). Therefore, measuring the electric

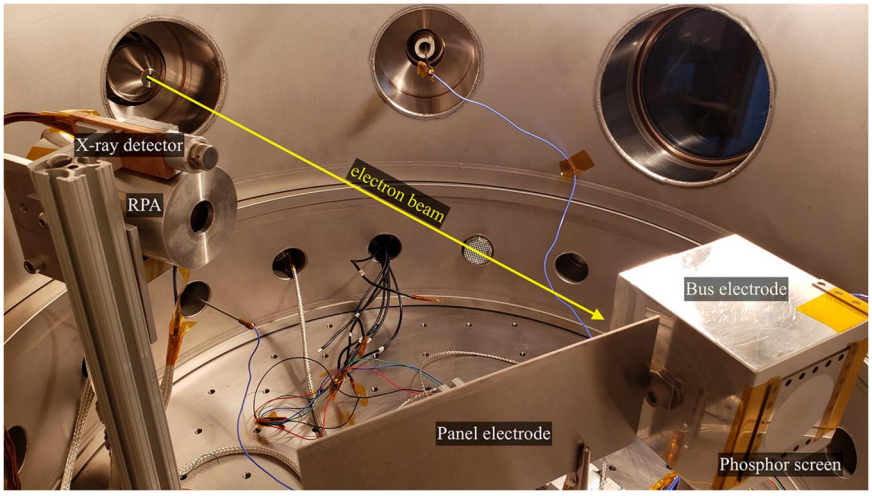

Fig. 2 Experimental setup with a box-and-panel object representing a spacecraft.

potential of the servicing satellite using a langmuir probe [19], knowing the initial electron beam energy, and estimating the landing energy of the electron beam from x-ray spectra, the potential of the target object can be inferred [18,21,23]. Note that no assumptions are made about the polarity of the electric potential of either the servicer or the target. In contrast to the electron method [17,20], the x-ray method also works for neutral or positively charged target objects. Regarding the servicer potential, it is assumed that it is being measured, and that the difference of electric potential between the servicer and the target is smaller than the electron beam energy. Otherwise, the electron beam is not energetic enough to reach the target. For the experiments conducted in the ECLIPS vacuum chamber, the electron gun is grounded, which corresponds to a neutral potential of the servicing satellite. Consequently, the change in energy of the electron beam is equal to the electric potential of the target object in the vacuum chamber. It should be noted that, in general, the electron beam affects the potential of a target object in space. This effect is considered out-of-scope for this work. In the conducted experiments, the potential of the target is controlled using high-voltage power supplies, so the potential of the target components remains nearly constant and is not affected by the electron beam.

B. Experimental Setup

The experiments are conducted in the ECLIPS Space Environments Simulation Facility [22]. The experimental setup is shown in Fig. 2 and consists of an electron beam, an x-ray detector, and a box-and-panel shaped object on a rotary stage representing a spacecraft bus with one solar panel. The bus of the spacecraft-like target object is a 70 mm × 70 mm × 70 mm cube and the panel is a 145 mm × 60 mm flat plate. Both components are made of aluminum. Additionally, a retarding potential analyzer (RPA) is included in the setup and used to touchlessly estimate potentials with the electron method [28], but is not required for the x-ray method. The electron beam is an EMG-4212C from Kimball Physics and capable of emitting electrons with energies from 1 to 30 keV and currents from 1 to 100 μA. The focus of the electron beam is adjustable, which allows to either hit a large area of the target object with electrons, or to focus the electron beam on a small spot. An Amptek X123 X-ray spectrometer with a 6 mm^2 Si-PIN diode is used to detect the x-rays, and the line between the x-ray detector and the test object approximately forms a 16° angle with the electron beam.

A Matsusada AU-30R1 and a Spellman SL300 high-voltage power supply separately control the potentials of the spacecraft bus and the panel, and are able to provide potentials up to 30 and 1 kV, respectively. The orientation of the spacecraft with respect to the electron beam is varied with an RM-3 vacuum compatible rotary stage from Newmark Systems, and measured with an incremental rotary high-vacuum Renishaw Tonic encoder. This angle is defined to be zero when the panel aligns with the electron beam. A Kimball Physics Rugged Phosphor Screen with a diameter of 3.8 cm is attached to the backside of the test object to verify the landing spot of the unperturbed electron beam (i.e., when both the bus and panel potential are grounded). The unperturbed landing spot of the electron beam is also used as a reference point for the setup of the numerical simulation with the particle tracing software described in the next section.

C. Particle Tracing Simulation Framework

A phosphor screen is used to center the electron beam for a specific orientation (−30°) of the uncharged target object, but the exact landing spot of the electron beam changes with the orientation of the object and the electric potential of the spacecraft bus and panel. However, to validate the experimental results, it is important to know if the electron beam is hitting the bus or panel, because both components are charged to different potentials. Thus, the particle tracing simulation software SIMION[¶] is configured to assist the interpretation of the experimental results. SIMION solves Laplace's equation to derive the electrostatic field and then computes the particle trajectory from Newton's second law. The implementation of the SIMION simulation framework for remote sensing of electric potentials is discussed in greater detail in Ref. [28]. Space-charge effects are not accounted for in the SIMION model, so the expansion of the electron beam and the effect of the electron beam on the electric field are neglected. As shown in Ref. [29], electrostatic repulsion is negligible for the beam divergence angles employed in the ECLIPS chamber, and the trajectory of the centroid of the beam depends only very weakly on beam repulsion. Because the main purpose of the SIMION model in this work is the validation of the beam landing spot, the implemented model is considered sufficiently accurate, and computationally more expensive models such as particle-in-cell (PIC) are not considered. The implication of neglecting space-charge is described further in Ref. [28]. The trajectories of the secondary electrons excited by the electron beam are also modeled in SIMION, but not shown or discussed here as they are irrelevant for the x-ray method. Figure 3 shows the SIMION model of the experimental setup.

III. Results

When measuring electric potentials using x-rays excited by an electron beam, the beam current, the energy, and the focus can be adjusted. A high beam current is generally desired, because it will result in more x-rays being generated and thus yields a stronger signal. However, one must take into account the possibility of detector saturation. The Amptek X123 X-ray spectrometer with a 6 mm^2 Si-PIN diode used in this work has a maximum count rate of 10,000

[¶]https://simion.com [retrieved 20 October 2022].

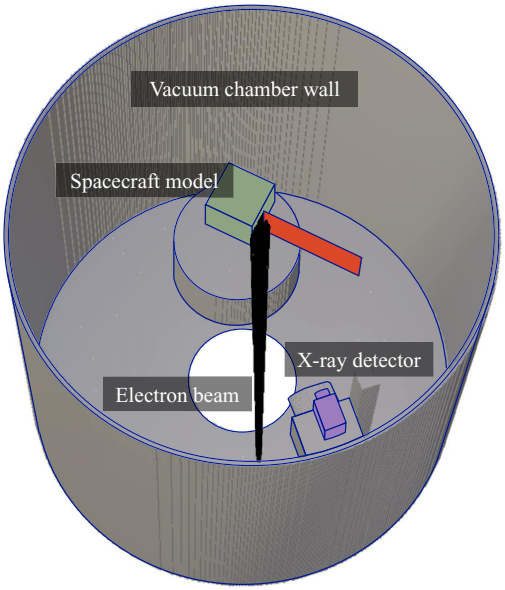

Fig. 3 SIMION model.

photons per second. Therefore, the electron beam current should be chosen such that this maximum count rate is not exceeded during the 20 s accumulation time frame of the x-ray detector. To stay below this limit, an electron beam current of 1 μA is used for all experiments in this work (see Sec. III.C.1 for more details). The code used for the data analysis rejects any recorded spectrum with a count rate that exceeds the maximum count rate of 10,000 photons per second, but this did not occur for any of the experiments. Naturally, the electron beam interacts with the electric field created by the charged target object and is deflected to some degree [29]. To reduce deflection, a high electron beam energy of $E_{\mathrm{EB}} = 10$ keV is used in this work. Finally, the electron beam focus is varied from experiment to experiment to provide either a narrow (half-cone angle of 0.2°), medium (0.5°), or a wide beam spot (2°). A narrow beam spot is used to excite x-rays from a small source region on the target object. Ideally, the electron beam hits only one spacecraft component for a given orientation and consequently each potential of a differentially charged object is measured individually. On the other hand, a wide beam spot is used to excite x-rays from multiple spacecraft components at once and thus measure multiple potentials simultaneously.

A. Measuring Each Component Individually

A small electron beam spot with a half-cone angle of about 0.2° is centered on the phosphor screen for a spacecraft angle of −30° and grounded components, as shown in Fig. 4. The half-cone angle θ is required for the SIMION simulations and is approximated by estimating the beam spot radius R_b on the phosphor screen and using

$$\tan\theta = \frac{R_b}{L_{t,eb}} \tag{1}$$

Fig. 4 Narrow electron beam for measuring each component individually.

where $L_{t,eb}$ is the distance from the electron beam source to the landing location. For the experiments, the angle of the target object is changed between −20° and 80° in 10° steps. The x-ray spectra are taken for a static target object orientation and using an x-ray accumulation time of 20 s, meaning that the x-ray detector counts photons for 20 s. Each experiment run is repeated five times.

Figure 5 shows some sample x-ray spectra for various target object angles. The electric potential of the bus is set to $\Phi_B = -500$ V and the potential of the panel is set to $\Phi_P = -1500$ V. To estimate the landing energy, it is not sufficient to simply take the energy of the highest energy photon observed by the x-ray detector due to the noise of the measurement. Instead, a more robust method is recommended by Ref. [30]. Taking advantage of the approximately linear shape of the Bremsstrahlung spectrum close to the landing energy, a linear curve is fitted to the upper energy part of the x-ray spectrum. The energy where this fitted line intersects the x axis corresponds to the estimated landing energy. This procedure is explained in greater detail in Refs. [21,23]. The fitted lines for each sample spectra are shown by the red curves in Fig. 5, labeled as *Estimate*. Note that the log-scale of the plot distorts the linear shape of the fitted Estimate line.

For a target object angle of −20°, the resulting x-ray spectrum includes characteristic peaks at approximately 5.4 and 6.4 keV. These peaks match with the characteristic energies of chromium (Cr, K_α transition at 5.41 keV) and iron (Fe, K_α transition at 6.4 keV) [31], indicating that the electron beam hits the stainless steel chamber wall. The estimated landing energy is approximately 10 keV. For an electron beam energy of 10 keV, this corresponds to an estimated potential of 0 V. This supports the claim that the beam is deflected from the target object and impacting on the chamber wall, because both electrodes are charged to nonzero potentials and the rest of the chamber is grounded. The x-ray spectra for an angle of 30° and 80° both include a characteristic peak at 1.5 keV, which agrees with the characteristic energy of aluminum (Al, K_α transition at 1.49 keV) provided by Ref. [31]. This suggests that the electron beam hits the aluminum target object. The estimated potential is approximately −1400 V for 30° and −500 V for 80°, indicating that the electron beam impacts on the panel for the former orientation and the spacecraft bus for the latter. If the target was charged to a positive potential, the landing energy of the electron beam electrons (and thus the maximum recorded x-ray energy) would be higher than the initial electron beam energy—opposed to being lower in the case of a negative target potential. Which object or component is observed in the x-ray spectrum for each orientation is confirmed by the simulated electron trajectories, as shown in Fig. 6.

The estimated potential as a function of the target object orientation is presented for two different voltage combinations in Figs. 7 and 8 using box-plots. The horizontal line inside of each box corresponds to the median of the data, and the bottom and top edges of the box represent the 25 and 75% percentiles. The black whiskers indicate the minimum and maximum of each data set, excluding outliers. Outliers are represented by circles and are values that are more than $1.5 \cdot IQR$ away from the bottom or top of the box, where IQR is the difference between the top and bottom box edges (interquartile range).

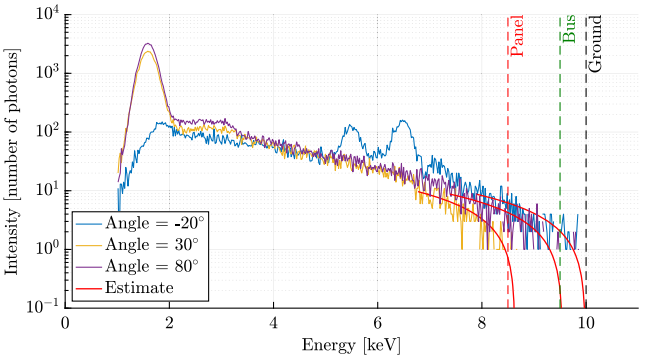

Fig. 5 X-ray spectra for different target object angles. $\Phi_B = -0.5$ kV, $\Phi_P = -1.5$ kV.

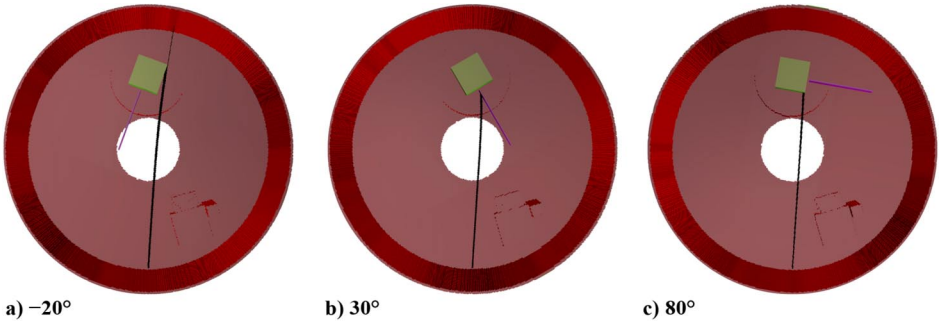

a) −20° b) 30° c) 80°

Fig. 6 Narrow beam trajectories from SIMION simulation. $\Phi_B = -0.5$ kV, $\Phi_P = -1.5$ kV.

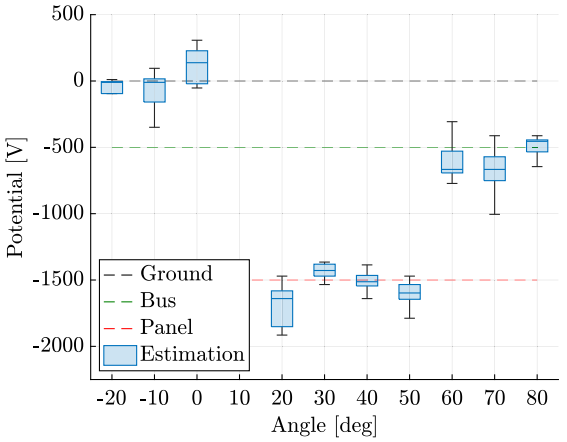

Fig. 7 Narrow beam results. $\Phi_B = -500$ V, $\Phi_P = -1500$ V.

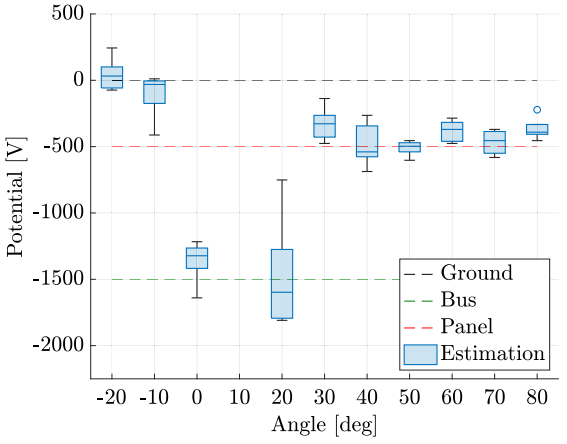

Fig. 8 Narrow beam results. $\Phi_B = -1500$ V, $\Phi_P = -500$ V.

Depending on the angle of the target object, the potential of the chamber wall, the bus, or the panel is measured. If the maximum photon count per energy bin is less than 100 photons, or the total number of photons counted is less than 1500 photons, the corresponding x-ray spectrum is rejected by the data analysis code due to an insufficient x-ray signal. This is the case for an angle of 10°, and the reason why Figs. 7 and 8 do not include any data for 10°. The consistent lack of signal at an angle of 10° over all experiment runs is a consequence of the experimental setup. As mentioned earlier, the x-ray detector and the electron beam are about 16° apart from each other, and the target object angle is defined as the angle between the panel and the source location of the electron beam. Thus, for an angle of 10°, the electron beam impacts on the panel on one side, but the x-ray detector is located on the other side of the panel, reducing the x-ray signal significantly. Even for an angle of 20°, the location of the detector is unfavorable, resulting in a weakened signal and consequently larger 2σ values. For angles below −10°, the electron beam is deflected and hits the chamber wall, and consequently the potential of the grounded chamber wall is measured. For the remaining angles, either the bus or panel potential is detected.

B. Target Observability

The previous subsection demonstrates that the orientation of the target object affects which component the electron beam impacts on and which potential is observed by the x-ray detector. The electric field due to the two electrodes varies from one orientation to the other, which changes the way the electron beam is deflected. Consequently, the landing spot of the electron beam is a function of the target object's orientation and the electric potential of its components. For low electric potentials as applied in this set of experiments (≤1.5 kV), however, the effect of the beam deflection is not as significant as the influence of the orientation of the target object. Which potential is measured essentially depends on the landing location of the beam. Table 1 provides an overview of which potential is measured by the x-ray detector, compared to the landing location of the electron beam as predicted by the SIMION simulation. The possible observations are the chamber wall (CW), the bus (B), the panel (P), both the bus and the panel (B/P), or loss of signal due to an insufficient number of photons (LOS). The outcome CW essentially means that the electron beam does not hit the spacecraft. Thus, in an in-orbit scenario, the outcome CW corresponds to a loss of signal.

In general, the observations by the x-ray detector agree well with the predictions by SIMION. For electrode configuration (a) and an angle of 40° − 50°, the x-ray detector measures the potential of the panel even though the SIMION simulation predicts the electron beam to hit both the bus and the panel. However, small modeling inaccuracies of the experimental setup geometry have a large effect on the accuracy of the SIMION simulation. Romero-Calvo et al. [28] show that there is a shift of about 3° between the experimental results for the electron method and the SIMION simulation, for the same chamber setup as in this

Table 1 X-ray observations: a) $\Phi_B = -0.5$ kV, $\Phi_P = -1.5$ kV; b) $\Phi_B = -1.5$ kV, $\Phi_P = -0.5$ kV

Configuration	Analysis	−20°	−10°	0°	10°	20°	30°	40°	50°	60°	70°	80°
a)	Experimental	CW	CW	CW	LOS	P	P	P	P	B	B	B
	SIMION	CW	CW	CW	LOS	P	P	B/P	B/P	B	B	B
b)	Experimental	CW	CW	B	LOS	B	P	P	P	P	P	P
	SIMION	B	CW	B	LOS	P	P	P	P	B/P	B	B

B, bus; B/P, both bus and panel; CW, chamber wall; LOS, loss of signal; P, panel.

work. Thus, this discrepancy is explained by geometric imprecisions of the SIMION chamber model. More interestingly, for electrode configuration (b) and angles between 60° and 80°, the potential of the panel is measured although the electron beam hits either the bus or both the bus and the panel in the SIMION simulation. In addition to an approximate SIMION chamber model, this is explained by the following phenomenon. If the electron beam impacts on two components charged to different potentials, then the electron landing energy is different for each component. However, only the higher landing energy is measured by the x-ray spectroscopy method explained in Sec. II.A. Thus, if the electron beam hits two components with dissimilar electric potentials, only the higher potential is measured, i.e., either the potential that is less negative or more positive. Because only negative potentials are used in the experiments within this work, only the potential that is smaller in magnitude is measured. For electrode configuration (b), this corresponds to the panel at $\Phi_P = -0.5$ kV.

C. Measuring Multiple Potentials Simultaneously

1. Theory

The analysis of target observability shows that, if the electron beam hits two components with different electric potentials, only the higher potential is detected when measuring the maximum photon energy to infer the electric potential per the Duane–Hunt law. This raises the question as to whether it is possible to measure multiple potentials simultaneously using a single x-ray spectrum. To investigate this, theoretical x-ray spectra are created for two different landing energies, representing two different potentials. Thick target x-ray models are used, meaning that it is assumed that the incident electrons are completely stopped in the target object. The average path length Δx traveled by a charged particle penetrating into a material is computed using the continuous-slowing-down-approximation (CSDA) [32]

$$\Delta x = \int_0^{E_0} \frac{1}{S(E)\rho}\,\mathrm{d}E \tag{2}$$

where E is the kinetic energy of the particle, E_0 is the initial kinetic energy as the particle impacts on the material, ρ is the density of the material, and $S(E) = -\mathrm{d}E/\mathrm{d}x$ is the linear stopping power on the particle. Using the NIST ESTAR database for electron stopping powers [33], one finds that a 20 keV electron is stopped within 4.3 μm of aluminum, which is much thinner than the 0.75 mm aluminum panel used in the experiments.

The model by McCall [34] is used to approximate the characteristic radiation of the theoretical spectrum. This model for the characteristic radiation is derived from x-ray tube measurements. The model assumes a thick target, the plasma temperature is lower than the incident electron energy, and there is no considerable ionization of the inner shell. The number of characteristic x-ray photons due to K_α transitions excited per incident electron with energy E_e is approximated by

$$I_{\mathrm{ph},c}(E_e) = \begin{cases} N\left(\frac{E_e}{E_k} - 1\right)^\alpha & \text{if } E_e \geq E_k \\ 0 & \text{if } E_e < E_k \end{cases} \tag{3}$$

where the parameters N, α, and the characteristic energy E_k are material dependent. For aluminum, $N = 1.4 \cdot 10^{-5}$, $\alpha = 1.63$, and $E_k = 1.49$ keV [34]. Since the characteristic energy E_k is the energy of the emitted characteristic photons, the energy of the incoming electron E_e must be greater than E_k to excite characteristic photons. Even though characteristic x-rays are emitted at a discrete energy, the x-ray detector senses a Gaussian distribution with a width defined by the full width at half maximum (FWHM). For the detector used in this work, the FWHM is approximately 140 eV and is converted to the standard deviation of the Gaussian distribution by

$$\sigma = \frac{\mathrm{FWHM}}{2\sqrt{2\ln(2)}} \tag{4}$$

Given the standard deviation and the number of characteristic photons per incident electron with energy E_e, the theoretical characteristic radiation as observed by the detector is computed using the normal distribution

$$I_{\mathrm{ph},c,\mathrm{det}}(E, E_e) = \frac{I_{\mathrm{ph},c}(E_e)}{\sigma\sqrt{2\pi}} \exp\left(-\frac{(E - E_k)^2}{2\sigma^2}\right) \tag{5}$$

The integral of this Gaussian distribution is $I_{\mathrm{ph},c}(E_e)$, so the number of photons per incident electron is redistributed from a discrete energy E_k to a Gaussian distribution with standard deviation σ.

The Bremsstrahlung spectrum is approximated using an empirical model for thick targets from Ref. [35] that is based on experiments with a normal incidence of the electron, and is valid for photon energies E ranging from 0.25 to 20 keV and atomic numbers Z between 4 and 83. After a few interactions of the incident electron with the atoms in the material, the electron path and the incidence electron direction are uncorrelated [35], so using a model that is based on normal incidence is considered applicable. This effect is also demonstrated in Ref. [23], where no correlation between the orientation of the target object and the accuracy of the x-ray method was found. With this model, the number of Bremsstrahlung x-ray photons with energy between E_e and $E_e + \Delta E$ (with bin size ΔE) excited per incident electron with energy E_e is estimated by

$$\begin{aligned} I_{\mathrm{ph},b}(E, E_e) = C\sqrt{Z}\frac{E_e - E}{E}\Bigg(&-73.90 - 1.2446E \\ &+ 36.502\ln(Z) + \frac{148.5E_e^{0.1293}}{Z}\Bigg) \\ &\cdot \left(1 + (-0.006624 + 0.0002906E_e)\frac{Z}{E}\right)\Delta E \end{aligned} \tag{6}$$

using a scaling factor of $C = 3.35 \cdot 10^{-7}$. The total number of photons N_{ph} with an energy of E that is sensed by the detector during an accumulation time of Δt is computed by

$$N_{\mathrm{ph}}(E, E_e) = \frac{I_{\mathrm{EB}}}{q}\Omega[I_{\mathrm{ph},c,\mathrm{det}}(E, E_e) + I_{\mathrm{ph},b}(E, E_e)]\Delta t \tag{7}$$

where I_{EB} is the electron beam current, and $q = 1.602176634 \cdot 10^{-19}$C is the elementary charge. The solid angle Ω is determined by $\Omega = (A_{\mathrm{det}}/L^2)$, with the detector area A_{det} and the distance of the detector from the x-ray source L. Finally, the efficiency of the x-ray detector is considered. Low-energy photons are filtered out by the Beryllium frontal window of the detector, while high-energy photons might not deposit a significant amount of their energy when transiting through the detector. To account for the attenuation of these photons, the energy-dependent efficiency curve of the x-ray detector is applied for the computation of the theoretical x-ray spectrum.** Using Eq. (7) with an approximate distance between the detector and the x-ray source of 25 cm, one finds that an electron beam current $I_{\mathrm{EB}} = 1$ μA yields a count rate of about 10,000 photons per second for a beam energy of 10 keV and a grounded target object. This justifies the choice of the 1 μA beam current that is used for all experiments, as a high photon count rate is desired while staying below the 10,000 photons per second detector saturation limit, as described at the beginning of Sec. III.

Figure 9 shows the individual theoretical spectra for landing energies of 10 and 7 keV. For an electron beam energy of 10 keV, this corresponds to electric potentials of 0 V and −3 kV, respectively. If an electron beam hits two components charged to different potentials at the same time, then the resulting total spectrum is obtained by superimposing the individual spectra of each landing energy. This is illustrated in Fig. 9c for potentials of 0 V and −3 kV, assuming that the same number of electrons impact both components. A discontinuity in the slope is produced in the total spectrum at an energy of 7 keV, which corresponds to the landing energy of the lower-energy

**https://www.amptek.com/products/x-ray-detectors/sipin-x-ray-detectors/sipin-x-ray-detectors [retrieved 20 October 2022].

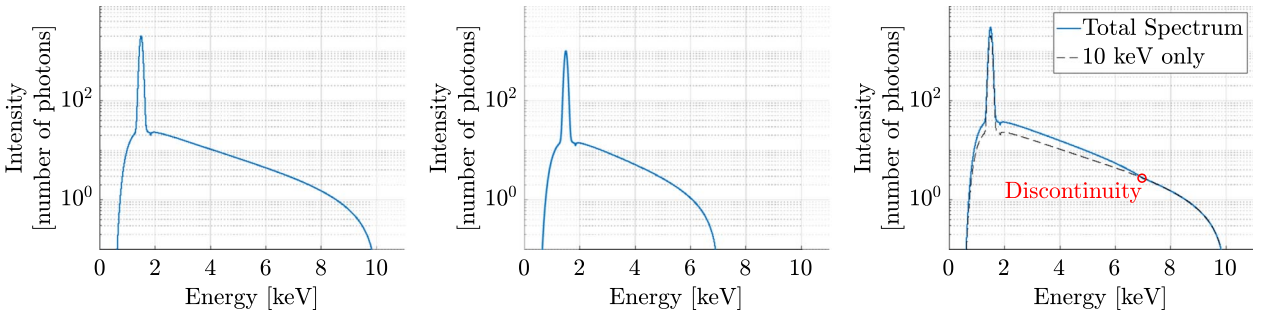

a) 10 keV spectrum **b) 7 keV spectrum** **c) Total spectrum**

Fig. 9 Theoretical superposition of x-ray spectra.

individual spectrum. Thus, the lower potential can be estimated by locating this discontinuity in the total spectrum, while the higher potential is estimated from the maximum photon energy of the spectrum (Sec. II.A).

In a real x-ray spectrum, however, this discontinuity is not easily identified due to the noise in the spectrum. Instead, the higher potential is estimated from the maximum photon energy of the total spectrum, and a theoretical spectrum is computed using the corresponding estimated landing energy. Subtracting the theoretical spectrum from the total spectrum yields a residual spectrum that approximates the individual spectrum of the lower potential component. The lower potential is then estimated by finding the maximum photon energy of the residual spectrum. For example, in Fig. 9, one would estimate the maximum photon energy from the total spectrum (Fig. 9c) and compute the corresponding higher landing energy spectrum (Fig. 9a). The residual spectrum (Fig. 9b) then provides an estimation of the lower landing energy. The two potentials are inferred from the two estimated landing energies.

2. *Experiments with Wide Electron Beam*

To investigate the proposed method experimentally, a wide electron beam spot with a half-cone angle of about 2° is centered on the phosphor screen for a spacecraft angle of −30° and grounded components, as shown in Fig. 10. For the experiments, the angle of the target object is changed between −20° and 80° in 10° steps. The x-ray spectra are taken for a static target object orientation and using an x-ray accumulation time of 20 s. Each experiment run is repeated five times.

For this experiment, a target object orientation must be found where the electron beam impacts on both the bus and the panel. SIMION shows that, for electrode potentials of $\Phi_B = 0$ kV and $\Phi_P = -3$ kV, the beam hits both components if the angle is 30° and only the bus if the angle is 80°, as shown in Fig. 11.

A spectrum for 80° is presented in Fig. 12a. The maximum photon energy of about 10 keV is determined using a linear curve fit in the higher energy part of the spectrum as described above. For a beam energy of 10 keV, this corresponds to a potential of 0 kV, i.e., the potential of the spacecraft bus. A theoretical x-ray spectrum is computed for the estimated landing energy of about 10 keV using

Fig. 10 Wide electron beam for measuring multiple potentials simultaneously.

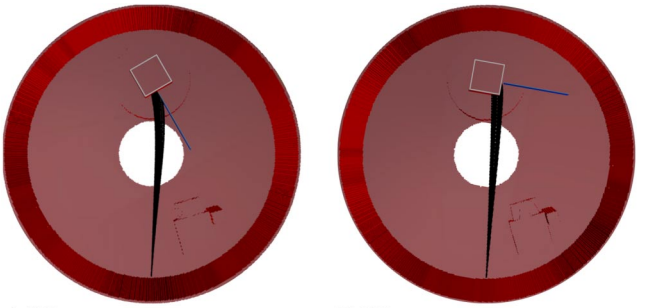

a) 30° **b) 80°**

Fig. 11 Wide beam trajectories from SIMION simulation. $\Phi_B = 0$ V, $\Phi_P = -3000$ V.

the models provided in Sec. III.C.1. The computed theoretical spectrum agrees well with the measured spectrum (Fig. 12a), and the resulting residual spectrum (the difference between the measured and theoretical spectrum, Fig. 12b) is low in intensity. This suggests that only one potential is detected, and that is the bus potential of 0 kV. Note that the lower limit of the y axis in Fig. 12 is 1 as this is the smallest nonzero number of photons that can be measured by the detector. The theoretical number of photons, however, can be a fraction of a photon. Thus, even though the theoretical curve in Fig. 12a intersects the x axis at about 9 keV (indicating a potential of −1 kV), it approaches an intensity of 0 photons at about 10 keV, corresponding to a potential of 0 kV (compare with Fig. 9). The experimental result is also confirmed by numerical simulations with SIMION that show that the beam only impacts the spacecraft bus for an orientation of 80° (Fig. 11b). No theoretical spectrum is shown in Fig. 12b due to the lack of a notable residual spectrum. A low-pass filtered curve of the data is plotted to illustrate the trend of the data.

The intensity of the theoretical x-ray spectrum needed to match the recorded spectrum is not exactly known. While it could be computed in theory using Eq. (7), such approximation depends on several factors, such as the number of electrons impacting the target, the distance between the x-ray source location and the detector, and the solid angle field of view of the detector. It also assumes that no structures of the target object block the x-ray detector field of view of the source region. These variables are uncertain in a real application, especially if the x-rays are emitted from multiple sources with different potentials, and an accurate intensity of the theoretical spectrum is crucial for the proposed method. Thus, instead of computing the intensity theoretically, the right scaling factor β of the intensity is determined by minimizing the root-mean-squared error between the actual spectrum and theoretical spectrum. The fitting region is a 1.5 keV window in the upper end of the spectrum. For example, if the estimated landing energy is 10 keV, then the fitting region is between 8.5 and 10 keV. However, this imposes limits on the detection of differential charging. For a fitting window of 1.5 keV, potential differences less than 1.5 kV cannot be detected. This also limits how many different potentials can be detected. Only six 1.5 keV windows fit into a spectrum with a maximum energy of 10 keV, restricting the theoretical number of potentials that can be detected to six. The

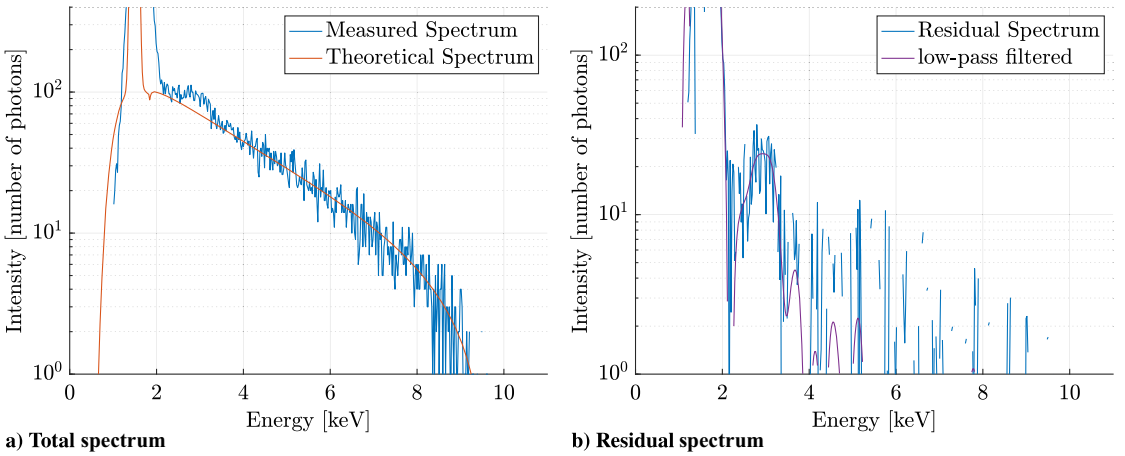

a) Total spectrum **b) Residual spectrum**

Fig. 12 Sample spectrum for 80°. $\Phi_B = 0$ kV, $\Phi_P = -3$ kV.

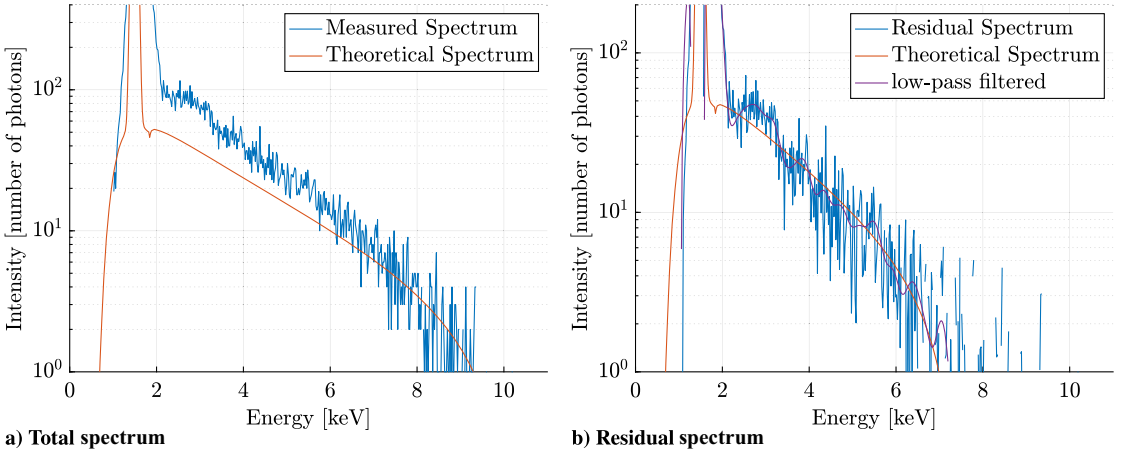

a) Total spectrum **b) Residual spectrum**

Fig. 13 Sample spectrum for 30°. $\Phi_B = 0$ kV, $\Phi_P = -3$ kV.

attenuation of low-energy x-rays within the x-ray detector likely decreases this number even further. Characteristic peaks inside the fitting window can be removed using the Matlab function findpeaks to avoid any interference of the peaks with the fitting process. This procedure is recommended in Ref. [21] to filter out characteristic radiation from the bremsstrahlung radiation.

Figure 13a shows a spectrum for 30°, where the electron beam impacts on both the bus and the panel. The maximum photon energy is determined and the corresponding theoretical spectrum computed. Here, the measured spectrum clearly deviates from the theoretical one. The residual spectrum in Fig. 13b is relatively high in intensity and approximately resembles an individual x-ray spectrum including both characteristic radiation and Bremsstrahlung radiation. The estimated landing energy for the residual spectrum is approximately 7 keV, which yields an estimated potential of about −3 kV. Using the estimated landing energy, another theoretical spectrum is computed.

The estimated potential as a function of the target object orientation for the given electrode configuration ($\Phi_B = 0$ kV, $\Phi_P = -3$ kV) is presented in Fig. 14. Estimation 1 employs the total measured spectrum and always measures the highest potential (least negative or most positive potential). Estimation 2 uses the residual spectrum. No second estimation is performed if the intensity of the residual spectrum is below a certain threshold between 2 and 4 keV, as this is an indicator that likely no second potential is present in the recorded spectrum (in this context, the second potential is the more negative potential). A threshold of 15 photons per energy was found to be effective for the given experimental setup, but might have to be adjusted for a different electron beam current, accumulation time, and distance between the x-ray source and the detector, as this affects the intensity of the measured spectrum. This means that the residual spectrum is rejected and no second estimation is performed if the low-pass filtered residual spectrum is

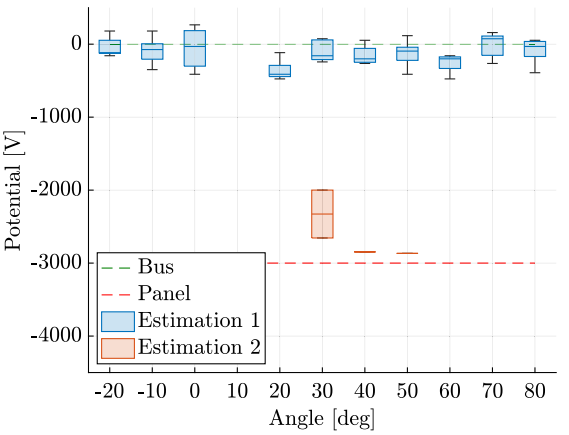

Fig. 14 Wide beam results. $\Phi_B = 0$ V, $\Phi_P = -3000$ V.

below 15 photons at some point between 2 and 4 keV. Alternatively a relative threshold could be used, e.g., 1% of the maximum intensity of the recorded spectrum. The first estimation always measures the highest potential, which is equal to 0 kV. When the beam impacts on both target object components (30°), the second estimation measures the lower potential of −3 kV. The low intensity of the residual spectrum results in a bad signal-to-noise ratio, which is disadvantageous for estimating the electric potential and likely the reason for the low accuracy of the second estimation. For orientations of 40° and 50°, all but one residual spectra are rejected due to low intensity, and the corresponding boxplots consist of only a horizontal line representing the single second estimation attempted for that angle.

The results suggest that it is possible to detect two potentials simultaneously with a single x-ray spectrum, using a theoretical Bremsstrahlung model. The theoretical model depends on the atomic number of the target element, so the material of the target must either be known or identified by the characteristic peaks of the measured spectrum. However, the occasion of an electron beam simultaneously hitting multiple components charged to different potentials is rather rare and highly dependent on the geometry of the target object and the electric field. A more realistic scenario is that the electron beam impacts multiple spacecraft components of a rotating object during a given sensing interval. Here a beam is moving across the spacecraft surface and exciting surface elements at different potentials in a sequential rather than parallel manner.

3. *Dynamic Experiments with Rotating Object*

All experiments in prior electric potential sensing work were static, meaning that the target object did not move while the x-rays were counted with the detector. Objects in space such as retired or uncooperative satellites might tumble with rotational rates of several degrees per second [36,37] due to solar radiation pressure or impacts of micro-meteoroids, which motivates dynamic experiments with rotating target objects. This is especially interesting for measuring multiple potentials simultaneously as the electron beam moves from one component to another during the sensing time frame.

An electron beam spot with a half-cone angle of about 0.5° is centered on the phosphor screen for a spacecraft angle of −30° and grounded components. The target object is rotated 30° with different starting angles, and the stepper motor speed is chosen such that this takes about 20 s. While the object is rotating, an x-ray spectrum is recorded using an accumulation time of 20 s, meaning that x-rays of all energies between a few eV and 20 keV are recorded simultaneously during a time frame of 20 s. Thus, if the electron impacts different components during the rotation of the target object, the resulting x-ray spectrum includes x-rays excited from both components. Experiments are performed with starting rotation angles between 0° and 80°, in 10° steps. Each experiment is repeated 20 times.

Figure 15 illustrates the electron beam trajectories for a bus potential of $\Phi_B = -3$ kV and a panel potential of $\Phi_P = -1$ kV. For angles up to about 70° − 80°, the electron beam impacts only on the panel. At about 80°, the beam transitions to the spacecraft bus, and at 110° the beam impacts only on the bus. Angles above 110° are not possible for the given experimental setup, as the spacecraft panel comes too close to the chamber wall.

The experiments conducted for this section include a bus potential of −3 kV and panel potentials of 0 and −1 kV. Figure 16 shows the estimated potential for a bus potential of −3 kV and panel potential of −1 kV as a function of the orientation of the target object. Estimation 1 accurately measures the potential of the spacecraft panel over all angles. Estimation 2 measures the potential of the cube for higher angles, where the beam impacts the cube. The reason why the second estimation is not as accurate is the low intensity of the residual spectrum. In one case (40° − 70°), a second estimation is attempted for one of the 20 samples, even though no second potential should be detected for these angles. Figure 17 shows the experimental results for a bus potential of −3 kV and panel potential of 0 kV. The results

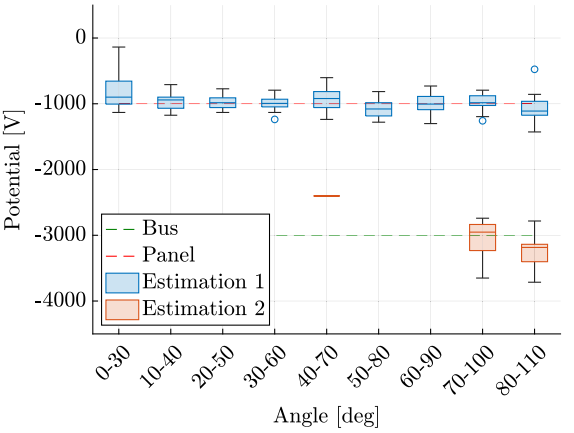

Fig. 16 Dynamic experiment results. $\Phi_B = -3000$ V, $\Phi_P = -1000$ V.

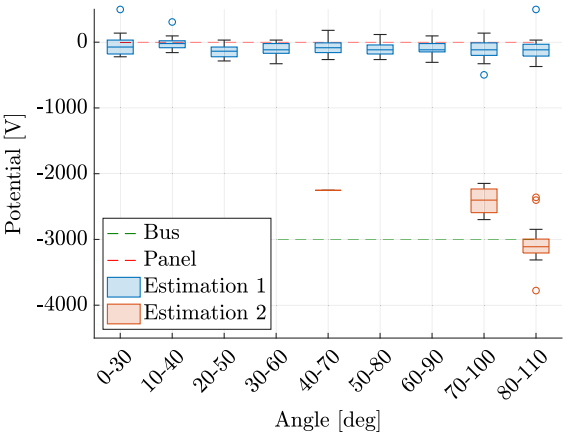

Fig. 17 Dynamic experiment results. $\Phi_B = -3000$ V, $\Phi_P = 0$ V.

are similar to Fig. 16. The first estimation measures the potential of the panel relatively accurately, while the second estimation is less accurate due to the low intensity of the residual spectrum. In both Figs. 16 and 17, the presence of a second potential is detected for orientations between 70° and 110°.

To detect the presence of multiple potentials in a realistic scenario of application, the electron beam needs to irradiate the corresponding component for a sufficient amount of time. This determines how fast the target spacecraft can rotate such that a measurement is still possible. Some of the residual spectra of the experiments here introduced have a total number of photons as low as $N_{\text{min}} = 20{,}000$. Taking this as the minimum required value for the residual spectrum to detect the second potential, the maximum rotational rate is determined by the flux of photons arriving at the detector. Using the theoretical x-ray models provided in Sec. III.C.1 and Eq. (7) with a distance between the detector and the target of $L = 15$ m and a detector area of $A_{\text{det}} = 70$ mm^2, a count rate of about $f = 3400$ photons per second is found for an electron beam current of

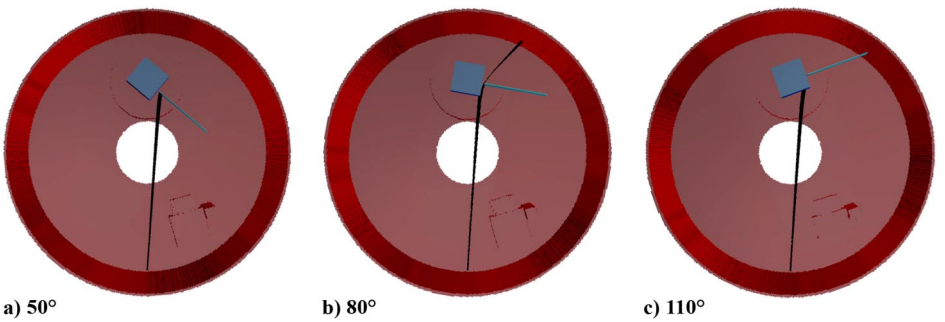

a) 50° b) 80° c) 110°

Fig. 15 Beam trajectories for dynamic experiment from SIMION simulation. $\Phi_B = -3$ kV, $\Phi_P = -1$ kV.

$I_{EB} = 100\ \mu$A and a beam energy of 10 keV. Therefore, the target spot needs to be irradiated for at least $t_{min} = N_{min}/f = 5.9$ s. Assuming for simplicity a spherical aluminum spacecraft of $R_{SC} = 1$ m radius and a characteristic cocentered beam spot radius of $R_b = 1.5$ cm at 15 m [29], the maximum rotational rate that allows the collection of x-ray photons from a small component with a width of $L_t = 20$ cm located on the equator of the sphere becomes

$$\omega_{max} = \frac{(L_t + 2R_b)/t_{min}}{R_{SC}} \tag{8}$$

which returns 2.2 deg/s for the problem under consideration. Larger components will be irradiated for longer times, increasing the maximum allowed rotational rate. A silicon drift detector (SSD) with an area of 70 mm^2 is the largest x-ray detector available from Amptek and is capable of count rates over 1,000,000 counts per second.[††] The maximum rotational rate can be increased by using several detectors to increase the effective detector area. In the case of the experimental setup used in this work, the beam impacts the cube (the component with the second potential) over more than 20 deg, allowing for rotational rates of more than 5 deg/s with a 6 mm^2 detector and a beam current of 1 μA.

IV. Conclusions

This work investigates the estimation of electric potentials of complex-shaped differentially charged objects using x-ray spectroscopy. The test object is a spacecraft shape primitive with two components that are charged to different potentials. The particle tracing software SIMION is used to support the analysis of the experiments by verifying the electron beam landing spot.

The experiments show that the orientation of the target object and the deflection of the electron beam affect the landing location of the electron beam. This is also confirmed by numerical simulations with SIMION. Thus, the orientation of the object affects which component's potential is measured. Using a focused electron beam with a small landing spot size helps to excite x-rays from only one component at a time. For such an electron beam configuration and a nonrotating object, several x-ray spectra taken from different angles are required to measure the potential of multiple components.

To estimate multiple potentials simultaneously from a single x-ray spectrum, the beam must hit multiple components during the sensing time frame. This is achieved by either a wide electron beam that excites x-rays from multiple components simultaneously, or by a rotating target object that causes the beam to impact on different components over time. However, with the conventional x-ray spectroscopic method that was proposed in prior work and used in this work (see Sec. II.A), only the higher potential of the two components can be measured; i.e., only the potential that is either less negative or more positive is detected. A new method is proposed that uses theoretical x-ray models and the principle of superposition of individual x-ray spectra to measure multiple potentials using a single recorded x-ray spectrum. Experiments are conducted with a rotating target object to excite x-rays from multiple components during the sensing time frame, demonstrating that this new method can be used for simultaneous measurements. This is promising for the electric potential estimation of tumbling objects where the landing location of the electron beam changes during the recording time frame. Moreover, the results suggest that the presence of a second potential in the recorded x-ray spectrum does not interfere with the estimation of the higher potential.

Acknowledgments

The authors would like to thank Kieran Wilson for fruitful discussions on the x-ray method and the setup and operation of the vacuum chamber experiment. This work was supported by the U.S. Air Force Office of Scientific Research under grant FA9550-20-1-0025. Álvaro Romero-Calvo thanks the *la Caixa* Foundation (ID 100010434, agreement LCF/BQ/AA18/11680099) and the Rafael del Pino Foundation for their financial support.

[††]https://www.amptek.com/products/x-ray-detectors/fastsdd-x-ray-detectors-for-xrf-eds/fastsdd-silicon-drift-detector [retrieved 20 October 2022].

References

[1] Lai, S. T., *Fundamentals of Spacecraft Charging*, Princeton Univ. Press, Princeton, NJ, 2011, Chaps. 1, 7. https://doi.org/10.2307/j.ctvcm4j2n

[2] Olsen, R. C., "Record Charging Events from Applied Technology Satellite 6," *Journal of Spacecraft and Rockets*, Vol. 24, No. 4, 1987, pp. 362–366. https://doi.org/10.2514/3.25925

[3] Garrett, H. B., and Whittlesey, A. C., *Guide to Mitigating Spacecraft Charging Effects*, Wiley, Hoboken, NJ, 2012, Chap. 3. https://doi.org/10.1002/9781118241400

[4] Katz, I., Davis, V., and Snyder, D., "Mechanism for Spacecraft Charging Initiated Destruction of Solar Arrays in GEO," *36th AIAA Aerospace Sciences Meeting and Exhibit*, AIAA Paper 1998-1002, 1998. https://doi.org/10.2514/6.1998-1002

[5] Brandhorst, H., and Rodiek, J., "Improving Space Utilization by Increasing Solar Array Reliability," *AIAA SPACE 2007 Conference and Exposition*, AIAA Paper 2007-6024, 2007. https://doi.org/10.2514/6.2007-6024

[6] Newman, C. P., Davis, D. C., Whitley, R. J., Guinn, J. R., and Ryne, M. S., "Stationkeeping, Orbit Determination, and Attitude Control for Spacecraft in Near Rectilinear Halo Orbits," *Proceedings of the AAS/AIAA Astrodynamics Specialist Conference 2018*, AAS Paper 2018-0388, 2018, https://ntrs.nasa.gov/citations/20180006800

[7] Wilson, K., and Schaub, H., "Impact of Electrostatic Perturbations on Proximity Operations in High Earth Orbits," *Journal of Spacecraft and Rockets*, Vol. 58, No. 5, 2021, pp. 1293–1302. https://doi.org/10.2514/1.A35039

[8] Hammerl, J., and Schaub, H., "Debris Attitude Effects on Electrostatic Tractor Relative Motion Control Performance," *Proceedings of the AAS/AIAA Astrodynamics Specialist Conference*, AAS Paper 2021-548, 2021, http://hanspeterschaub.info/Papers/Hammerl2021a.pdf.

[9] Wilson, K., Romero-Calvo, Á., and Schaub, H., "Constrained Guidance for Spacecraft Proximity Operations Under Electrostatic Perturbations," *Journal of Spacecraft and Rockets*, Vol. 59, No. 4, 2022, pp. 1–13. https://doi.org/10.2514/1.A35162

[10] Schaub, H., and Moorer, D. F., "Geosynchronous Large Debris Reorbiter: Challenges and Prospects," *Journal of the Astronautical Sciences*, Vol. 59, Nos. 1–2, 2012, pp. 161–176. https://doi.org/10.1007/s40295-013-0011-8

[11] Hammerl, J., and Schaub, H., "Effects of Electric Potential Uncertainty on Electrostatic Tractor Relative Motion Control Equilibria," *Journal of Spacecraft and Rockets*, Vol. 59, No. 2, 2022, pp. 552–562. https://doi.org/10.2514/1.A35165

[12] Ferguson, D. C., Murray-Krezan, J., Barton, D. A., Dennison, J. R., and Gregory, S. A., "Feasibility of Detecting Spacecraft Charging and Arcing by Remote Sensing," *Journal of Spacecraft and Rockets*, Vol. 51, No. 6, 2014, pp. 1907–1913. https://doi.org/10.2514/1.A32958

[13] Bennett, T. J., "On-Orbit 3-Dimensional Electrostatic Detumble for Generic Spacecraft Geometries," Doctoral Thesis, Univ. of Colorado, Boulder, CO, 2017, http://hanspeterschaub.info/Papers/grads/TrevorBennett.pdf.

[14] Engwerda, H. J. A., "Remote Sensing for Spatial Electrostatic Characterization Using the Multi-Sphere Method," Master's Thesis, Delft Univ. of Technology, Delft, The Netherlands, 2017, http://hanspeterschaub.info/Papers/grads/HeikoEngwerda.pdf.

[15] Stevenson, D., and Schaub, H., "Multi-Sphere Method for Modeling Spacecraft Electrostatic Forces and Torques," *Advances in Space Research*, Vol. 51, No. 1, 2013, pp. 10–20. https://doi.org/10.1016/j.asr.2012.08.014

[16] Fahleson, U., "Theory of Electric Field Measurements Conducted in the Magnetosphere with Electric Probes," *Space Science Reviews*, Vol. 7, Nos. 2–3, 1967, pp. 238–262. https://doi.org/10.1007/BF00215600

[17] Bengtson, M., Hughes, J., and Schaub, H., "Prospects and Challenges for Touchless Sensing of Spacecraft Electrostatic Potential Using Electrons," *IEEE Transactions on Plasma Science*, Vol. 47, No. 8, 2019, pp. 3673–3681. https://doi.org/10.1109/TPS.2019.2912057

[18] Wilson, K., and Schaub, H., "X-Ray Spectroscopy for Electrostatic Potential and Material Determination of Space Objects," *IEEE Transactions on Plasma Science*, Vol. 47, No. 8, 2019, pp. 3858–3866. https://doi.org/10.1109/TPS.2019.2910576

[19] Brace, L. H., "Langmuir Probe Measurements in the Ionosphere," *Geophysical Monograph-American Geophysical Union*, Vol. 102, Jan. 1998, pp. 23–36.
https://doi.org/10.1029/GM102p0023

[20] Bengtson, M. T., Wilson, K. T., and Schaub, H., "Experimental Results of Electron Method for Remote Spacecraft Charge Sensing," *Space Weather*, Vol. 18, No. 3, 2020, pp. 1–12.
https://doi.org/10.1029/2019SW002341

[21] Wilson, K. T., Bengtson, M. T., and Schaub, H., "X-ray Spectroscopic Determination of Electrostatic Potential and Material Composition for Spacecraft: Experimental Results," *Space Weather*, Vol. 18, No. 4, 2020, pp. 1–10.
https://doi.org/10.1029/2019SW002342

[22] Wilson, K., Romero-Calvo, Á., Bengtson, M., Hammerl, J., Maxwell, J., and Schaub, H., "Development and Characterization of the ECLIPS Space Environments Simulation Facility," *Acta Astronautica*, Vol. 194, July 2022, pp. 48–58.
https://doi.org/10.1016/j.actaastro.2021.12.037

[23] Wilson, K. T. H., "Remote Electrostatic Potential Determination for Spacecraft Relative Motion Control," Doctoral Thesis, Univ. of Colorado, Boulder, CO, 2021, http://hanspeterschaub.info/Papers/grads/KieranWilson.pdf.

[24] Wilson, K., Hammerl, J., and Schaub, H., "Using Plasma-Induced X-ray Emission to Estimate Electrostatic Potentials on Nearby Space Objects," *Journal of Spacecraft and Rockets*, Vol. 59, No. 5, 2022, pp. 1–4.
https://doi.org/10.2514/1.A35161

[25] Bengtson, M. T., Wilson, K., and Schaub, H., "Broad-Spectrum Electron Gun for Laboratory Simulation of Orbital Environments," *Proceedings of the AIAA SciTech 2021 Forum and Exposition*, AIAA Paper 2021-1539, 2021.
https://doi.org/10.2514/6.2021-1539

[26] Reimer, L., *Scanning Electron Microscopy*, 2nd ed., Springer Series in Optical Sciences, Springer, Berlin, 1998, Chap. 10.
https://doi.org/10.1007/978-3-540-38967-5

[27] Duane, W., and Hunt, F. L., "On X-Ray Wave-Lengths," *Physical Review*, Vol. 6, No. 2, 1915, pp. 166–172.
https://doi.org/10.1103/PhysRev.6.166

[28] Romero-Calvo, Á., Hammerl, J., and Schaub, H., "Touchless Potential Sensing of Differentially Charged Spacecraft Using Secondary Electrons," *Journal of Spacecraft and Rockets*, Vol. 59, No. 5, 2022, pp. 1–11.
https://doi.org/10.2514/1.A35355

[29] Romero-Calvo, Á., Cano-Gómez, G., and Schaub, H., "Simulation and Uncertainty Quantification of Electron Beams in Active Spacecraft Charging Scenarios," *Journal of Spacecraft and Rockets*, Vol. 59, No. 3, 2022, pp. 739–750.
https://doi.org/10.2514/1.A35190

[30] Lamoureux, M., and Charles, P., "General Deconvolution of Thin-Target and Thick-Target Bremsstrahlung Spectra to Determine Electron Energy Distributions," *Radiation Physics and Chemistry*, Vol. 75, No. 10, 2006, pp. 1220–1231.
https://doi.org/10.1016/j.radphyschem.2006.06.006

[31] Deslattes, R. D., Kessler, E. G., Jr., Indelicato, P., de Billy, L., Lindroth, E., Anton, J., Coursey, J. S., Schwab, D. J., Chang, C., Sukumar, R., Olsen, K., and Dragoset, R. A., "X-Ray Transition Energies," Ver. 1.2, National Inst. of Standards and Technology, Gaithersburg, MD, 2005, http://physics.nist.gov/XrayTrans [retrieved 23 Nov. 2022].

[32] Berger, M. J., and Seltzer, S. M., "Stopping Powers and Ranges of Electrons and Positrons," National Bureau of Standards, Washington, D.C., 1982, https://ui.adsabs.harvard.edu/abs/1982spre.reptR....B.

[33] Berger, M. J., Coursey, J. S., Zucker, M. A., and Chang, J., "ESTAR, PSTAR, and ASTAR: Computer Programs for Calculating Stopping-Power and Range Tables for Electrons, Protons, and Helium Ions," Ver. 1.2.3, National Inst. of Standards and Technology, Gaithersburg, MD, 2005, http://physics.nist.gov/Star [retrieved 23 Nov. 2022].

[34] McCall, G. H., "Calculation of X-ray Bremsstrahlung and Characteristic Line Emission Produced by a Maxwellian Electron Distribution," *Journal of Physics D: Applied Physics*, Vol. 15, No. 5, 1982, pp. 823–831.
https://doi.org/10.1088/0022-3727/15/5/012

[35] Trincavelli, J., and Castellano, G., "The Prediction of Thick Target Electron Bremsstrahlung Spectra in the 0.25–50 keV Energy Range," *Spectrochimica Acta Part B: Atomic Spectroscopy*, Vol. 63, No. 1, 2008, pp. 1–8.
https://doi.org/10.1016/j.sab.2007.11.009

[36] Šilha, J., Pittet, J.-N., Hamara, M., and Schildknecht, T., "Apparent Rotation Properties of Space Debris Extracted from Photometric Measurements," *Advances in Space Research*, Vol. 61, No. 3, 2018, pp. 844–861.
https://doi.org/10.1016/j.asr.2017.10.048

[37] Papushev, P., Karavaev, Y., and Mishina, M., "Investigations of the Evolution of Optical Characteristics and Dynamics of Proper Rotation of Uncontrolled Geostationary Artificial Satellites," *Advances in Space Research*, Vol. 43, No. 9, 2009, pp. 1416–1422.
https://doi.org/10.1016/j.asr.2009.02.007

C. Hartzell
Associate Editor